



Super-adsorptive and photo-regenerable carbon nanotube based membrane for highly efficient water purification

Yang Yang^{a,1}, Zhu Xiong^{a,**,1}, Zhu Wang^{a,1}, Yi Liu^{b,1}, Zijun He^a, Akun Cao^c, Li Zhou^d, Lijing Zhu^e, Shuaifei Zhao^{f,*}

^a Key Laboratory for Water Quality and Conservation of the Pearl River Delta, Ministry of Education, School of Environmental Science and Engineering, Guangzhou University, Guangzhou, Guangdong, 510006, PR China

^b Key Laboratory of Marine Materials and Related Technologies, Zhejiang Key Laboratory of Marine Materials and Protective Technologies, Ningbo Institute of Materials Technology and Engineering, Chinese Academy of Sciences, Ningbo, 315201, China

^c Institute of Civil Engineering, Guangzhou University, Guangzhou, Guangdong, 510006, PR China

^d Key Laboratory of New Processing Technology for Nonferrous Metal and Materials (Ministry of Education) and College of Materials Science and Engineering, Guilin University of Technology, Guilin, 541004, China

^e Ningbo Institute of Materials Technology and Engineering, Chinese Academy of Sciences, Ningbo, Zhejiang, 315201, PR China

^f Institute for Frontier Materials, Deakin University, Geelong, Victoria, 3216, Australia

ARTICLE INFO

Keywords:

Adsorbents
Carbon nanotube
Catalytic membrane
-cleaning
Wastewater treatment

ABSTRACT

Carbon nanotube (CNT) based adsorbents have attracted extensive research interest for aqueous pollutants removal. However, such adsorbents face the problems of limited adsorption capacities and costly regeneration. Here, we report a highly adsorptive photo-regenerable CNT based multifunctional membrane with excellent self-cleaning properties via the facile vacuum filtration method, followed by FeOOH in-situ anchoring and silver-amino reaction. Various dyes (Rhodamine B, methylene blue, eosin Y and acid orange 7) and emerging contaminants (bisphenol A, amoxicillin and p-nitrophenol) were tested with the CNT based membrane. Our membrane exhibited superior adsorption performance to dyes among CNT based adsorbents reported in literature. In particular, the CNT based composite membrane displayed even better adsorption performance to cationic dyes. The adsorption capacities of the membrane for Rhodamine B and methylene blue were up to 181 and 247 mg/g, respectively. The membrane also had excellent self-cleaning and photo-regenerable properties after severe organic fouling. Our multifunctional CNT based membrane combined the features of adsorption, membrane separation, and catalytic degradation into one system, showing great promise for dye polluted wastewater purification. This study also offers a new strategy to engineer robust adsorptive, self-cleaning and regenerable membranes for wastewater treatment.

1. Introduction

Water pollution by various organic and inorganic contaminants from industrial, agricultural and pharmaceutical wastewater has worsened the global challenge of water scarcity [1–3]. Among these contaminants, dyes [4], pharmaceuticals [5], and pesticides [6] have been often detected in drinking water. After disinfecting, some organic contaminants transfer into highly toxic disinfection by-products via chlorine substitution or addition reaction, inducing acute or chronic diseases for humans or animals [7,8]. Therefore, developing advanced treatment

technologies for efficient organic contaminants removal is of special interest and great importance. Various methods, such as coagulation/flocculation, adsorption, advanced oxidization processes (AOPs) and membrane filtration, have been implemented to reduce organic contaminants [9–12].

Among these methods, membrane separation has been recognized as the next generation of water purification and reclamation technology due to its high separation efficiency, continuous and simple operation, less chemical requirements, modularity and low footprint [9,13]. However, highly selective pressure driven membranes capable of

* Corresponding author.

** Corresponding author.

E-mail addresses: xiongzhu@gzhu.edu.cn (Z. Xiong), s.zhao@deakin.edu.au (S. Zhao).

¹ These authors contributed equally to this work.

removing organic micropollutants are often dense, and require high hydraulic pressure and thus high energy consumption [14,15]. Membrane distillation and forward osmosis could be promising for removing organic micropollutants due to their minimal pressure requirements, but the former is limited to non-volatile organic micropollutants [16] and the latter requires regeneration of the draw solution [17]. Meanwhile, traditional membranes suffer from fouling during long-term operation, leading to temporary or permanent declines in flux and rise in energy consumption [18]. Therefore, new membrane materials preparation and design have been widely studied to overcome the trade-off between water purification efficiency and energy consumption.

Carbon nanotubes (CNTs) are promising materials for water purification. CNTs have been used as adsorbents [19] and catalyst-supports [20] in AOPs for various wastewater treatment applications. CNTs have been combined with different materials to form nanocomposites, such as CNTs-bentonite [21], CNTs-graphene [20], and CNTs-magnetic graphene [22] for pollutants adsorption. Reactive metals and oxides of Fe, Ti, Cu, or Mn have also been employed to load on CNTs, thereby inducing diverse superoxides to produce highly reactive oxygen species (ROs), such as hydroxyl radical ($\cdot\text{OH}$) and/or superoxide radical ($\text{O}_2\cdot^-$) [20,23]. The reactive radicals can degrade a wide range of toxic organic pollutants into harmless mineralized salts, carbon dioxide, and water, leading to the regeneration of CNTs. However, the adsorption capacity of CNTs based adsorbents are limited, and CNTs supported catalysis requires chemicals for ROs generation and catalysts regeneration. On the other hand, CNTs as powders tend to cause serious recontamination and face recycling issues [24,25].

CNTs based membranes have been regarded as attractive candidates for water purification [26,27]. CNT membranes with interweaved nanoporous structures have been fabricated by a combination of self-assembly and simple filtration methods [28,29]. Ultrathin free-standing CNTs network membranes were also developed via the facile vacuum filtration method for separation of emulsified oil/water mixture. However, most of these CNT membranes were used for water purification based on their adsorptive or rejection properties, in which membrane fouling and performance regeneration are the key challenges [18,30,31]. In addition, these CNT membranes cannot be used to remove trace organic contaminants with relatively small molecular weights from drinking water due to their large pore sizes.

Engineering adsorptive and catalytic CNT based membranes would solve the disadvantages of conventional CNT based adsorbents and membranes mentioned above, and lead to highly efficient removal of organic micropollutants due to the synergetic effect of physical adsorption and chemical catalysis [32,33]. In this work, we developed an interweaved super-adsorptive and photo-regenerable CNT based membrane for highly efficient water purification. First, a highly adsorptive CNT membrane was prepared by dispersing single wall CNT powders in a water solution followed by vacuum filtration. The CNT membrane was then used as a support to anchor photocatalytic FeOOH catalysts on the outer walls of CNTs, endowing the CNT based membrane with excellent self-cleaning properties via photo-induced Fenton-like oxidation. Finally, to improve the membrane stability under practical conditions, we utilized the electroless welding method [34] to produce silver nano-knots between the adjacent interweaving CNTs by the silver-ammonia reaction. The adsorption, dynamic filtration, and photo-regeneration (i.e. self-cleaning) performances of the CNT based membranes in water purification were evaluated using different model pollutants (e.g. Rhodamine B, methylene blue, and eosin Y). This study provides a new strategy to engineer multifunctional high performance membranes with adsorptive and self-cleaning properties for water purification and wastewater reclamation.

2. Experimental

2.1. Materials and chemicals

Electrospun polypropylene (PP) flat-sheet membranes (mean pore size 0.22 μm , thickness $\sim 8 \mu\text{m}$, SEM images were shown in Fig. S1) from Haining Kewei Filtration Equipment Co. Ltd. (Zhejiang, China) were used as the support for CNT filtration. Single-walled CNTs (diameters 10–30 nm; lengths 10–30 μm , purity > 99%) were purchased from Xianfeng Nano Materials Tech Co., Ltd (Jiangsu, China). Silver nitrate, ammonia solution, dimethyl formamide (DMF), ferrous sulfate tetrahydrate, hydrogen peroxide (H_2O_2 , 30 wt%), sodium hydroxide, glucose, 5,5-dimethyl-1-pyrroline-1-oxide (DMPO), albumin bovine serum (BSA), Rhodamine B (RhB), methylene blue (MB), eosin Y (EY) and acid orange 7 (AO7) were purchased from Aladdin Reagent Co., Ltd (Shanghai, China). High-toxic emerging contaminants, including bisphenol A (BPA), amoxicillin (AX) and p-nitrophenol (NP), were also purchased from Aladdin Reagent Co., Ltd (Shanghai, China) for the preparation of synthetic wastewater.

2.2. Fabrication of CNT based membranes

First, 0.02 g CNT powders were put into 20 mL DMF, and then ultrasonically mixed for 3 h to obtain a well-dispersed solution. CNTs were deposited on the PP membranes by vacuum filtration of the CNT-dispersed solution (-0.1 MPa). The pristine CNT membranes were then washed with deionized water for five times to remove residual DMF. And then, they were immersed into 10 mL ferrous sulfate tetrahydrate solution (6.7 g/L) for 24 h at 95 $^\circ\text{C}$. During this process, 10 mL 30 wt% H_2O_2 was dropwise added into the ferrous sulfate solution, which induced FeOOH nanomaterials growing on CNT to form CNT-M-FeOOH membranes. The prepared CNT-M-FeOOH membranes were then washed with deionized water for five times. Finally, the CNT-M-FeOOH membranes were dipped into the mixture solution containing 5 mL silver nitrate solution (0.1 wt%), 6 mL ammonia solution (0.2 wt%), 0.5 mL sodium hydroxide solution (1.0 wt%), and 17.2 mL glucose solution (0.5 wt%) for 5 min at room temperature. The Ag-CNT-M-FeOOH membrane was formed by silver-amino reaction [34]. The thickness of the prepared membranes was around 0.22 μm .

2.3. Membrane characterization and performance evaluation

The prepared CNT based membranes (marked as CNT-M, CNT-M-FeOOH and Ag-CNT-M-FeOOH) were characterized by scanning electron microscopy (SEM, FEI, Hillsboro, USA), energy dispersive spectroscopy (EDS, FEI Quanta FEG 250), Raman spectroscopy (LabRamHR Evolution, JR, France), Fourier transforms infrared spectroscopy (FTIR, Waltham, MA, USA), X-ray photoelectron spectroscopy (XPS, Waltham, MA, USA), atomic force microscopy (AFM, MFP-3D, America) and water contact angle measurement (WCA, DSA100, Kruss, Germany). The pore size and porosity of the membranes were evaluated by automatic mercury injector (Demo Autopore IV 9500, Micromeritics, Atlanta, GA, USA). A low field nuclear magnetic resonance (NMR) spectrometer (PDNMR20-015 V, Niumai Electronic Technology Ltd. Co., Suzhou, China) was used to determine the relaxation time of water molecules on membrane surfaces. Meanwhile, the pore size distribution of the membrane surfaces before and after photo-Fenton oxidation was analyzed by the low field NMR spectrometer. More details can be seen in the supplementary material.

Membrane separation performance was assessed using a crossflow filtration cell (round shape with a diameter of 4 cm) under a certain hydraulic pressure. Firstly, pure water fluxes of the membranes were tested by changing the hydraulic pressures (0.05 - 0.2 MPa). Each hydraulic pressure was maintained for 60 min. The membrane flux was calculated by Eq. (1). The ultrafiltration coefficients (K_{UF}) was calculated according to Eq. (2). A BSA solution (1 g/L) was also tested for 60

min under 0.1 MPa via the same crossflow system. The rejection to BSA ($R_e\%$) was obtained by Eq. (3) [35].

$$J = \frac{V}{S \times t} \quad (1)$$

where V is the permeate volume (L) within the operation time t (h), and S is the effective membrane area (7.1 cm^2).

$$K_{UF} = \frac{Q_{UF}}{TMP} \times \frac{1}{S} \quad (2)$$

where Q_{UF} is the flux, and TMP represents the transmembrane pressure.

$$R_e = \left(1 - \frac{C_t}{C_0}\right) \times 100\% \quad (3)$$

where C_t and C_0 are BSA solute concentrations of the permeate and feed solutions, respectively, measured with a UV-vis-NIR spectrometer (TU1810, Persee, China) at 278 nm.

Long-term continuous crossflow filtrations under 0.1 MPa were also performed using various dyes and toxic organics polluted water as the feeds, including RhB (20 ppm), MB (20 ppm), EY (20 ppm), AO7 (20 ppm), BPA(5 ppm), AM(5 ppm), and NP(5 ppm) for dynamic adsorption experiments. The volume of each feed solution was 1 L. The separation time lasted 180 min with the crossflow system under 0.1 MPa. The permeate through the CNT-based membranes was collected for testing. As a contrast, the static adsorption experiments were performed using the RhB polluted water as the feed solution. The three CNT-based membranes were immersed in 100 mL RhB solution (10 ppm) for 120 min. After every 30 min, the feed solution was tested to evaluate the static adsorption performance of the three CNT-based membranes. The removal efficiencies for small organics were obtained by Eq. (3), where solute concentrations of permeate and feed solutions were measured with UV-vis-NIR spectrometer (TU1810, Persee, China) at 554 nm for RhB, 664 nm for MB, 515 nm for EY, 485 nm for AO7, 276 nm for BPA, 228 nm for AM, and 317 nm for NP, respectively. The adsorption capability of the membrane was obtained according to Eq. (4).

$$q = \frac{(C_0 - C_t)V}{m} \quad (4)$$

where C_0 and C_t are the initial and real-time concentrations of pollutants in water after membrane separation, respectively, m is the weight of the CNT membrane, and V is the real-time volume of the feed solution.

To study the dynamic adsorption, the pseudo-first-order and pseudo-second-order kinetic models were applied to fit the experimental data [36]. The pseudo-first-order and pseudo-second-order kinetic models are as follows:

$$\frac{dq_t}{dt} = k_1(q_e - q_t) \quad (5)$$

$$\frac{dq_t}{dt} = k_2(q_e - q_t)^2 \quad (6)$$

where q_e and q_t are the adsorption capabilities at equilibrium and real-time (t), respectively. k_1 is the pseudo-first-order rate constant and k_2 is the pseudo-second-order rate constant. To find linear relations for these two kinetic models, they can be transformed by integration and presented as:

$$\text{Log}(q_e - q_t) = \text{Log}q_e - \frac{k_1}{e}t \quad (7)$$

$$\frac{t}{q_t} = \frac{1}{k_2q_e^2} + \frac{1}{q_e}t \quad (8)$$

Photocatalytic regeneration performance of the CNT membranes was evaluated by immersing organic-fouled Ag-CNT-M-FeOOH into ultrapure water containing H_2O_2 ($10 \mu\text{L}$ per 50 mL water) for photocatalysis

under the UV light ($\lambda = 420 \text{ nm}$) at room temperature for 60 min after each cycle of separation. The continuous filtration performance of the CNT membranes before and after photocatalysis was monitored to reveal the self-cleaning property of the membrane. The stability of Ag-CNT-M-FeOOH was evaluated according to the dynamic adsorption performance change after using the membranes in photocatalytic treatment for different times.

3. Results and discussion

3.1. Membrane fabrication and characterization

Combining CNTs with membranes has several advantages. First, CNTs can act as both adsorbents and catalyst-supports, imparting the membranes with excellent adsorptive and catalytic properties after loading with catalysts [19,20] for various wastewater treatment applications. Second, the CNT based catalytic membranes can not only degrade a wide range of toxic organic pollutants, but also reduce membrane fouling by the degradation-induced self-cleaning properties [37]. Last, selecting membranes as the support of CNTs can overcome the issues of powdered adsorbents, such as aggregation, recontamination and costly regeneration [28,38,39]. Therefore, we selected CNTs to prepare the adsorptive and catalytic substrate membranes.

Three CNT based membranes were prepared by the facile vacuum filtration method as schemed in Fig. 1a. SEM shows that CNTs interweaved with each other to form porous membrane structures (middle column of Fig. 1). After FeOOH anchoring, the CNT-M-FeOOH also had interweaved porous structures on the surface. There was little obvious structure difference between CNT-M and CNT-M-FeOOH based on the SEM images. However, EDX reveals that element Fe (red dot) was densely distributed on the surfaces of CNT-M-FeOOH and Ag-CNT-M-FeOOH (Fig. 1 (c2 and d2)), but little Fe was observed on the CNT-M membrane surface (Fig. 1b). It demonstrates that large quantities of FeOOH nanoparticles were successfully loaded on the CNT-M-FeOOH and Ag-CNT-M-FeOOH. Furthermore, to improve the structure stability of CNT-M-FeOOH, physical welding points were constructed via the silver-ammonia reaction (Fig. 1a) [34]. As shown in Fig. 1(d, d1), some obvious nanoparticles were tied by CNTs, suggesting the formation of welding points. Ag NPs were successfully fabricated as the welding points on the Ag-CNT-M-FeOOH and thus enhance the membrane stability. FeOOH and Ag NPs narrowed the pores of the interweaved membranes via in-situ growth and welding, leading to denser membrane surfaces (Fig. S2). As a result, after FeOOH and Ag NPs loading on the CNT membrane surface, the membrane surface became much smoother (Fig. S3). The surface roughness declined from 23 nm of the pristine CNT membrane to 15 nm of the Ag-CNT-M-FeOOH.

The compositions of the CNT based membranes (CNT, CNT-M-FeOOH, and Ag-CNT-M-FeOOH) were characterized by Raman spectrum and XPS. Raman spectra of the three CNT based membranes were displayed in Fig. 2a, showing the characteristic representatives of ordered and disordered carbon structures. The characteristic D band (1417 cm^{-1}), and G band (1595 cm^{-1}) were observed. The intensity ratios of the G band to the D band (I_G/I_D) can be used to evaluate the structural disorder degree of carbon materials [28,40]. Lower I_G/I_D values mean higher disordered degree of the carbon material. The calculated I_G/I_D values of CNT-M, CNT-M-FeOOH, and Ag-CNT-M-FeOOH were 20.5, 12.4, and 10.7, respectively (Fig. 2a). The defective (disorder) degrees of the CNT based membranes increased with the rise in FeOOH and Ag NPs loading because of their great interruption to the well-ordered sp^2 -hybridized CNTs.

XPS were utilized to detect the composition and chemical states of the CNT based membranes. As shown in Figs. 2b and 2c, 10.79% oxygen was present on the surface of the pristine CNT membrane. The oxygen levels increased to 22.65%, and 25.92% for CNT-M-FeOOH, and Ag-CNT-M-FeOOH, respectively. This is because the decoration of Ag on CNT-M-FeOOH resulted in a decrease of carbon. As a result, the Fe and O

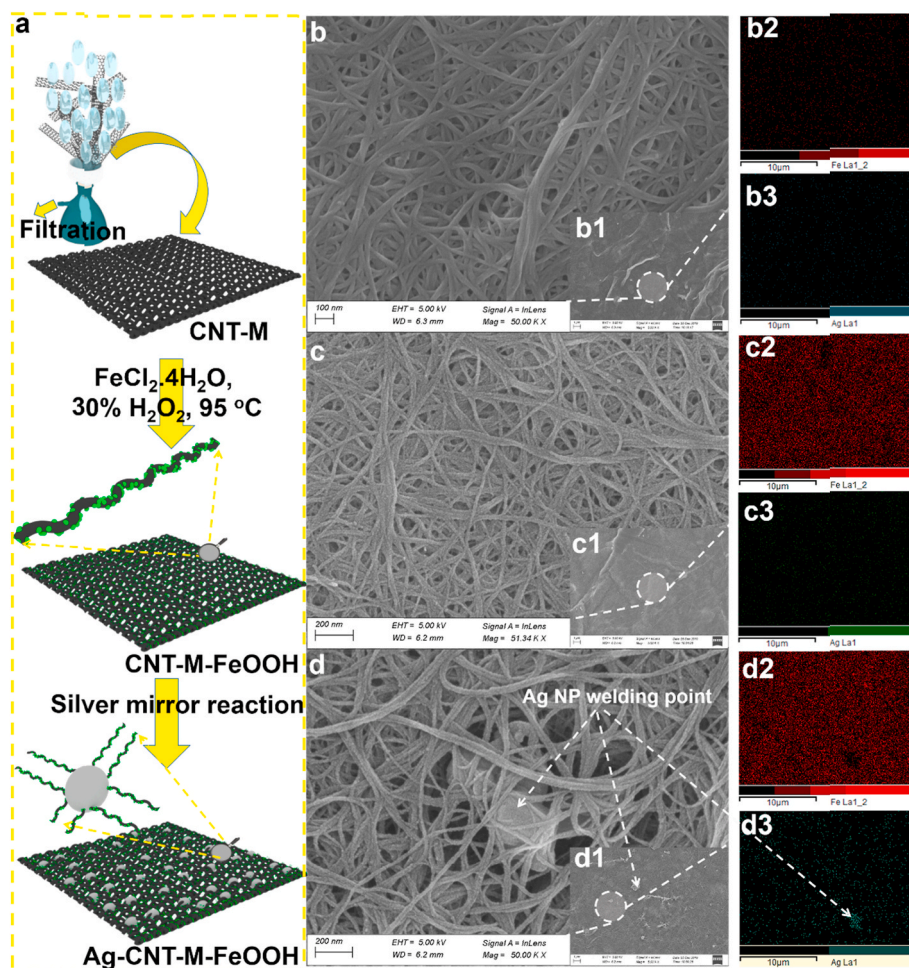


Fig. 1. The first column: (a) preparation procedure of the CNT based membranes. The middle column: SEM images of the three CNT based membranes (b1, c1 and d1) at different magnifications (50.00 and 5.00 KX). The last column: EDX mapping of the three CNT based membranes (the red color represents element Fe and the green color represents element Ag). (For interpretation of the references to color in this figure legend, the reader is referred to the Web version of this article.)

elements increased to make up the reduction of carbon. Moreover, the mirror reaction belongs to the redox reaction, which caused the distribution of O and Fe element change on the CNT membrane surface.

Meanwhile, 5.58%, and 8.37% iron atoms co-existed on CNT-M-FeOOH, and Ag-CNT-M-FeOOH, respectively, while no ion was detected on the pristine CNT-M. These results indicate the immobilization of FeOOH on both CNT-M-FeOOH and Ag-CNT-M-FeOOH. Because of the silver-ammonia reaction, only Ag-CNT-M-FeOOH possessed 1.17% silver among the three CNT based membranes (Fig. 2b). The high-resolution XPS spectra of Fe 2p for CNT-M-FeOOH and Ag-CNT-M-FeOOH (Fig. 2c) show typical characteristic peaks of FeOOH, with two main peaks located at 711.5 and 726.0 eV [41]. By peak-differentiating and imitating (Fig. 2c), the peak at 711.5 eV can be divided into two peaks at 711.1 eV assigning to Fe^{3+} , and 712.4 eV attributing to Fe^{2+} , further confirming the existence of FeOOH in the two membranes (CNT-M-FeOOH and Ag-CNT-M-FeOOH) [42].

Fig. 2d shows the XPS spectra of O 1s on the three CNT based membranes. In the pristine CNT membrane, only one peak at 532.6 eV from the C-O bond [43] was observed. The O 1s peaks on CNT-M-FeOOH and Ag-CNT-M-FeOOH changed significantly. The peak of the C-O bond shifted to 531.8 eV. The positive shifts (ca. 0.8 eV) of the C-O peak in binding energy reveal the electron interactions between FeOOH and CNT for both CNT-M-FeOOH and Ag-CNT-M-FeOOH [41]. Meanwhile, a new peak at 530.1 eV attributing to Fe-O-Fe bonds clearly appeared on CNT-M-FeOOH and Ag-CNT-M-FeOOH compared with the pristine CNT-M (Fig. 2d) [41,42]. In addition, after silver-ammonia reaction, the

Ag-CNT-M-FeOOH membrane showed two new characteristic peaks of Ag at 368.3 and 374.3 eV (Fig. 2e) [44], demonstrating the elementary Ag NPs growing or welding between the neighbored CNTs.

3.2. Membrane filtration performance

Pore size distributions of the three CNT based membranes were tested by a mercury injection apparatus. In Fig. 3a, after FeOOH in situ grew and Ag NPs welded, the pore size distribution of the membrane became narrow and shifted to the small position. Correspondingly, the mean pore diameter and porosity of CNT-M-FeOOH decreased to ~ 29 nm and $\sim 58\%$, which were lower than those (~ 36 nm and $\sim 62\%$) of the pristine CNT-M (Fig. 3b). FeOOH grew on the surface of CNT, leading to a tight connection between neighbored CNTs. The interweaved CNT-FeOOH membrane became dense with narrowed pores and reduced porosity. Afterwards, with silver-ammonia reaction, the mean pore size and porosity of the interweaved Ag-CNT-M-FeOOH further decreased to ~ 23 nm and $\sim 56\%$ due to the immobilization of Ag NPs on the membrane surface and their welding between the neighbored CNTs.

Essential ultrafiltration properties of the CNT based membranes were evaluated by the pure water flux and BSA rejection. Generally, the mean pure water flux of each CNT membrane has a linear relationship with the driven pressure (Fig. 3c). The pristine CNT-M exhibited much larger pure water flux than the two modified CNT membranes under the driven pressures ranging from 0.05 to 0.2 MPa. This is because that the water permeability of the membrane is mainly governed by its effective

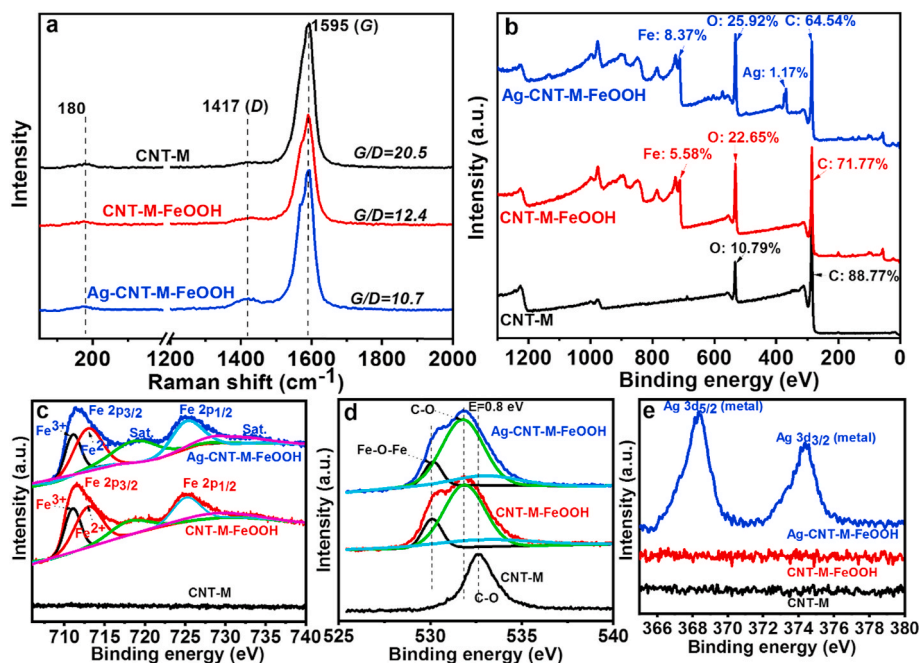


Fig. 2. (a) Raman spectra, and (b) XPS wide scans and elemental mass percentages of the three CNT based membrane surfaces. High-resolution XPS spectra of (c) Fe 2p, (d) O 1s, and (e) Ag 3d on the membrane surfaces.

average pore size. With the enlarging of the effective average pore size, the water permeability of the membrane increase. Interestingly, the water permeabilities of the two modified membranes (Ag-CNT-M-FeOOH and CNT-M-FeOOH) were similar (Fig. 3c). The improvement of water permeability of Ag-CNT-M-FeOOH could be attributed to its higher hydrophilicity (Fig. S4) [35].

In practical applications, membranes are often operated by pressures via crossflow systems to produce water. However, the trans-membrane pressure can exacerbate the adsorption of foulants on membrane surfaces and/or inside membrane pores, resulting in severe flux drops [18, 30,31]. The BSA filtration performance of the CNT based membranes was shown in Fig. 3d. During 60-min continuous filtration with CNT-M, the permeation flux declined dramatically from 53 to 39 L/m²·h, suggesting severe BSA fouling on the pristine CNT membrane surface and/or in its pores due to its largest pore size and porosity (Fig. 3b) as well as its highest initial flux. Fig. 3e exhibited the BSA rejection of the pristine CNT membrane increasing from 55% to 68% within 60 min. However, large quantities of BSA passed through the membrane, leading to a greater fouling risk in the membrane inner pores. Although Ag-CNT-M-FeOOH had smaller pore sizes (i.e. denser structures) as shown in Fig. 3b, its selectivity against BSA was lower than that of CNT-M-FeOOH (Fig. 3e). BSA molecules are much smaller than the membrane pores [45]. These results suggest that the size exclusion effect was not the dominant rejection mechanism of these membranes against BSA, while dynamic adsorption may play a more pronounced role in the selectivity.

For CNT-M-FeOOH and Ag-CNT-M-FeOOH, their flux stabilities significantly improved during dynamic filtration with BSA solution (Fig. 3d). The fluxes of CNT-M-FeOOH and Ag-CNT-M-FeOOH were maintained at ~23 L/m²·h and ~34 L/m²·h, respectively, during the 60-min continuous filtration. There results indicate that BSA fouling of CNT-M-FeOOH and Ag-CNT-M-FeOOH was formed in the beginning, but it did not exacerbate during the filtration. Although CNT-M-FeOOH had a larger pore size and porosity than Ag-CNT-M-FeOOH, the latter membrane showed a higher flux than the former membrane. This phenomenon may be caused by the higher hydrophilicity of Ag-CNT-M-FeOOH (Fig. S4). The better BSA rejections of CNT-M-FeOOH and Ag-CNT-M-FeOOH were also observed (Fig. 3e). Especially for CNT-M-

FeOOH, its BSA rejection reached 81% at the beginning, and then increased to ~92% after 60-min continuous filtration. The excellent BSA rejection of CNT-M-FeOOH may originate from the chelating effect of membrane surface-anchored FeOOH with BSA molecules [46]. Large quantities of BSA were firstly adsorbed on CNT-M-FeOOH surface to form a dense BSA cake layer as schemed in Fig. 3f. As a result, the BSA retention of CNT-M-FeOOH subsequently increased, resulting in fewer BSA molecules passing through the membrane inner pores and maintaining a relatively stable flux.

BSA rejection of Ag-CNT-M-FeOOH (from 58% to 86%) was lower than that of CNT-M-FeOOH (from 81% to 92%) during the 60-min filtration (Fig. 3e). This is because that, after the silver-amino reaction, some adsorption active sites of FeOOH were coated by Ag NPs, reducing the chelate effect with BSA. As a result, the Ag-CNT-M-FeOOH membrane displayed an intermediate BSA rejection performance between the pristine CNT membrane and CNT-M-FeOOH, although it had the smallest pore size and porosity. Ag-CNT-M-FeOOH also exhibited stable fluxes in continuous filtration with BSA solution.

Fig. 4a showed the continuous fluxes of the three CNT based membranes within 180 min. Because of the large pore size, the pristine CNT membrane displayed the largest initial flux (~300 L/m²·h) using 20 ppm RhB solution as the feed. However, our five repeats with the pristine CNT membrane shows that their flux stability could not be maintained more than 120 min. Even after 90 min, the fluxes of some CNT-M membranes increased sharply, suggesting the broken porous structure of the membrane. This demonstrated that a strong shear flow force detached or destroyed the pristine CNT membrane in the long-term continuous separation of RhB solution as scheme in Fig. 4d. After FeOOH in-situ growing, the flux of CNT-M-FeOOH declined due to its smaller pore size (Fig. 4a). However, all the CNT-M-FeOOH membranes maintained relatively stable flux for at least 120 min, implying that the in-situ coated FeOOH enhanced the interaction between the neighbored CNTs. Thus, the CNT-M-FeOOH membrane exhibited better resistance to long-term crossflow shear flow. However, the flux robustness of all CNT-M-FeOOH membranes could not withstand 140-min crossflow shearing due to the low membrane structural stability (Fig. 4d). The fluxes of all five Ag-CNT-M-FeOOH membranes were well maintained at ~125 L/m²·h even after 180-min filtration of RhB solution. This demonstrated

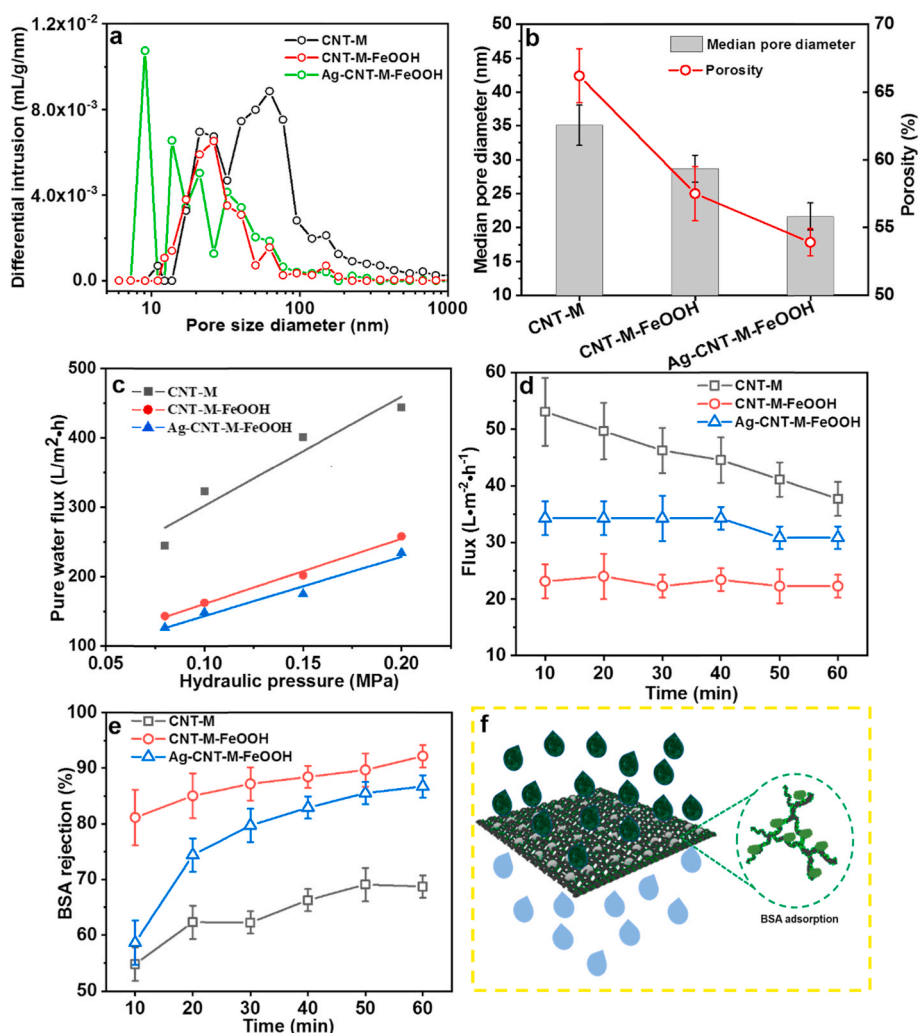


Fig. 3. (a) Pore size distributions, (b) mean pore sizes and porosities, (c) pure water fluxes, (d) fluxes with BSA solutions, and (e) BSA rejections of the three CNT based membranes (0.1 MPa; 1 g/L BSA). (f) Schematic illustration of BSA adsorption onto the Ag-CNT-M-FeOOH.

that the structural stability of Ag-CNT-M-FeOOH significantly improved (Fig. 4d). The silver-amino reaction resulted in many welding points between the neighbored CNTs on the Ag-CNT-M-FeOOH, which offered a promise for robust separation of dye-polluted water.

Fig. 4b exhibited the RhB removal efficiencies of the three CNT based membranes. For the pristine CNT membrane, its RhB removal maintained >90% at the initial 40 min. As shown in Movie. S1, a lot of visibly transparent fluid was collected in filtrate during the red feed solution permeating through the CNT membrane, indicating the high-efficient separation to RhB. Afterwards, RhB removal of CNT-M underwent a rapid decline to ~50% after 90-min due to the saturated adsorption of CNT-M (Fig. 4b). Fig. 4c showed that the RhB adsorption capacity of CNT-M arranged from 263 to 305 mg/g. For the CNT-M-FeOOH membrane (Fig. 4c), RhB removal was still above 90% after 70-min continuous separation, and slowly reduced to 69% in the following 50 min, indicating the improvement in RhB removal. However, the RhB adsorption capacity of CNT-M-FeOOH arranged from 205 to 227 mg/g, which was lower than that of the pristine CNT-M (Fig. 4c). These results were mainly caused by the reduced pore size and porosity of the membrane (Fig. 3b). After FeOOH loading, the adsorption active sites of CNTs reduced, leading to a reduction in the maximum RhB adsorption capacity of CNT-M-FeOOH. For the Ag-CNT-M-FeOOH membrane (Fig. 4c), its RhB removal maintained above 90% after 90 min. Even after 180 min, the RhB removal of Ag-CNT-M-FeOOH was still above 60%, indicating the excellent RhB removal robustness in the long-term

filtration. Nevertheless, the maximum RhB adsorption capacity of Ag-CNT-M-FeOOH further declined to ~181 mg/g. After silver-amino reaction, many Ag NPs were decorated on CNTs or FeOOH, which shielded some adsorption active sites of the membrane, lowering the adsorption capacity of the membrane. These results indicated that there was a trade-off between structural stability and adsorption capacity for the CNT based membranes in dynamic separation of dye polluted water.

In addition, we investigated the static removal efficiencies of the three CNT based membranes for adsorption of RhB as schemed in Fig. S5a. Fig. S5b showed the RhB removal and adsorption capacity during 120-min static adsorption. The pristine CNT-M only displayed 7% removal efficiency and 6.8 mg/g adsorption capacity for RhB even after 120 min. The hydrophobicity of pristine CNT-M caused very slow diffusion of RhB inside the membrane pores in the static condition [47]. The RhB adsorption mainly occurred on the membrane surface. As discussed in Fig. S4, there was no obvious change in hydrophilicity between CNT-M-FeOOH and CNT-M. Thus, the CNT-FeOOH membrane exhibited similar adsorption behaviors with the pristine CNT membrane (Fig. S5b). RhB molecules were much easier to diffuse into the more hydrophilic Ag-CNT-M-FeOOH membrane surface, evidenced by the higher RhB adsorption capacity (Fig. S5b). However, the maximum RhB adsorption capacities of the three CNT based membranes in static adsorption were much lower than those in dynamic adsorption (8 vs. 180 mg/g). The single molecular size of RhB (<2 nm [48]) was much smaller than the membrane pore size (Fig. 3b). The extremely low static

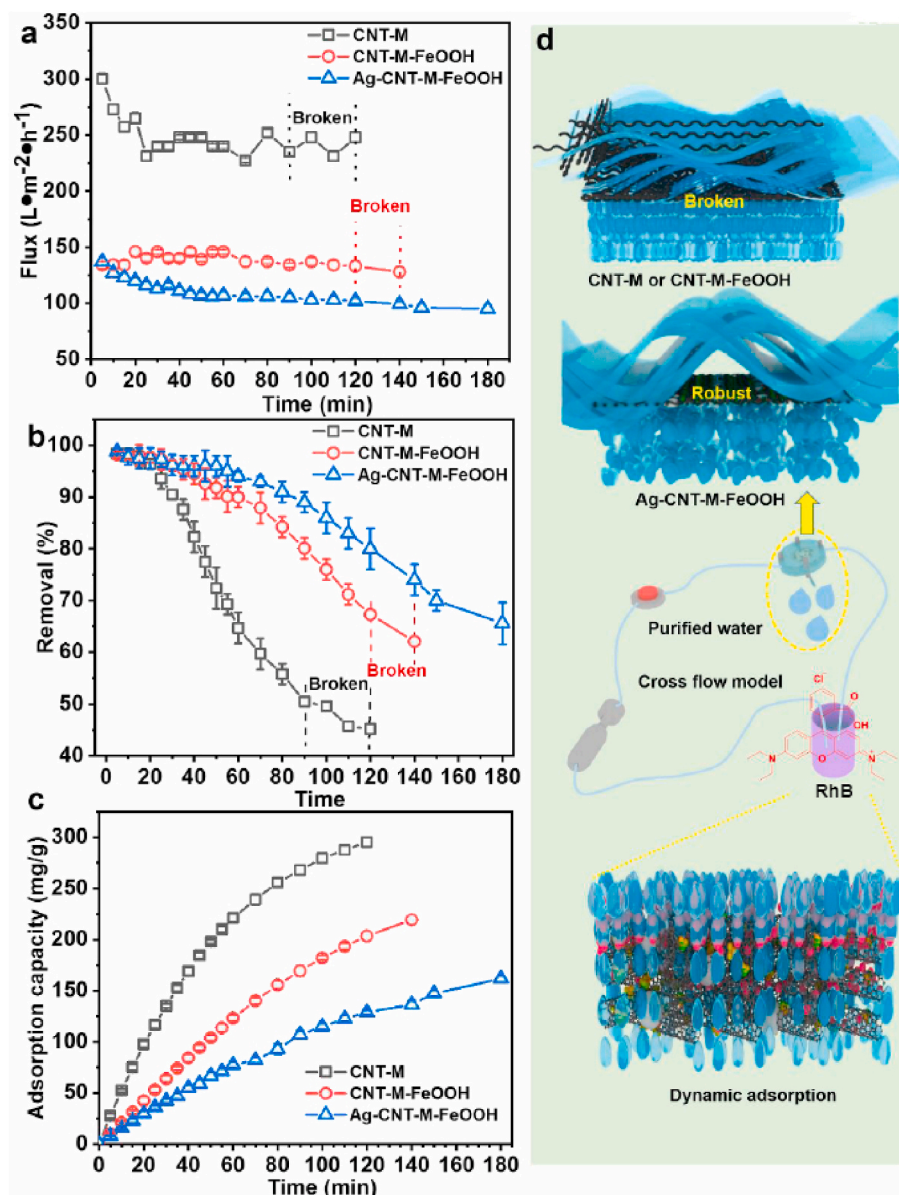


Fig. 4. (a) Permeation fluxes, (b) removal efficiencies, and (c) adsorption capacities of the three CNT based membranes for dynamic crossflow separation of RhB solution (20 ppm) at 0.1 MPa. (d) Schematic diagrams of CNTs detaching from CNT-M or CNT-M-FeOOH, and stable Ag-CNT-M-FeOOH with highly efficient adsorption under vigorous crossflow shearing.

adsorption performance suggested severe aggregation of the RhB molecules. The high dynamic adsorption performance indicated that crossflow filtration can break through the diffusion limitation of water-soluble dye pollutants, leading to effective adsorption of water-soluble micropollutants by the active sites of the membrane.

3.3. Membrane dynamic adsorptive and photo-regenerative performance

The regenerability and stability of membrane adsorption is an essential factor for its practical application. Re-generable CNT membranes are highly desirable for both fundamental research and practical applications. As schemed in Fig. 5a, multi-regeneration of Ag-CNT-M-FeOOH was implemented via the photo-catalytic treatment in the presence of trace H₂O₂. The nature of the photo-Fenton oxidation of Ag-CNT-M-FeOOH was studied using the ESR spin-trap technique [49]. Fig. 5b showed that no peaks occurred in the magnetic field of the CNT and CNT-M, indicating no reactive•OH species generated on their surfaces while contacting H₂O₂ under UV irradiation. However, several

obvious peaks due to reactive•OH species appeared in the magnetic field for CNT-M-FeOOH [50]. FeOOH is a promising heterogeneous photo-Fenton catalyst because it has a low band gap to provide photo-catalytic sites for the generation of reactive•OH species in the presence of H₂O₂ [43,51,52]. After silver-amino reaction, the peaks from reactive•OH species were still presented in the magnetic field for Ag-CNT-M-FeOOH under the same testing conditions (Fig. 5b). The immobilization of Ag NPs had no significant influence on the photo-catalytic sites of CNT-M-FeOOH. Therefore, the Ag-CNT-FeOOH membrane showed excellent photocatalytic efficiency for removing organic foulants from the membrane adsorption sites under UV irradiation in the presence of H₂O₂.

The Raman spectrum was used to detect the photocatalytic cleaning of Ag-CNT-M-FeOOH after saturated adsorption with RhB (Fig. 5c). The saturated adsorption of RhB induced a large scale of broad peaks on the Raman spectrum of Ag-CNT-M-FeOOH due to its fluorescent effect [53], resulting in the shielding of characteristic peaks of the pristine Ag-CNT-M-FeOOH membrane. After 30-min photo-Fenton treatment,

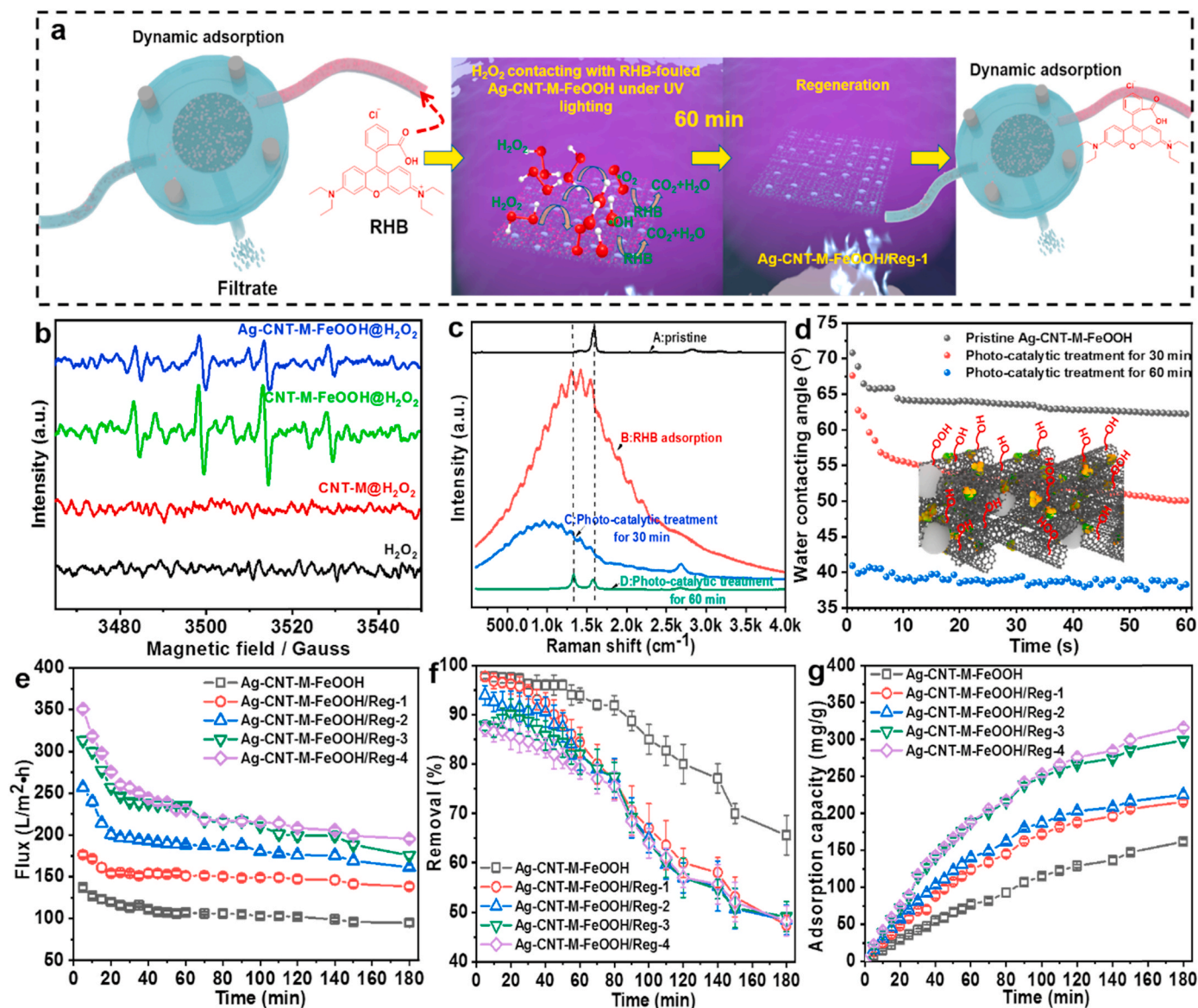


Fig. 5. (a) Schematic diagram of the regeneration of Ag-CNT-M-FeOOH via photo-catalytic treatment. (b) DMPO spin-trapping ESR spectra of hydroxyl radicals recorded for the three membranes after photo-catalytic treatment with trace H₂O₂. (c) Raman spectra of Ag-CNT-M-FeOOH under different conditions, including pristine, adsorption saturation, photo-catalytic treatments for 30 and 60 min. (d) Water contact angle changes of Ag-CNT-M-FeOOH under different conditions, including pristine, photo-catalytic treatments for 30 and 60 min. (e) Permeation fluxes, (f) removal efficiencies, and (g) adsorption capacities of regenerated Ag-CNT-M-FeOOH during 180-min filtration with 20 ppm RhB.

the broad peaks of the RhB-fouled Ag-CNT-M-FeOOH membrane were largely reduced (Fig. 5c), indicating the photocatalytic efficiency for RhB removal. With the time of photo-Fenton treatment increasing to 60 min, the broad peaks of the RhB-fouled Ag-CNT-M-FeOOH membrane completely disappeared (Fig. 5c). Meanwhile, the Raman spectrum of the RhB-fouled Ag-CNT-M-FeOOH membrane was almost recovered to its pristine status. These results demonstrated the regeneration of the Ag-CNT-M-FeOOH membrane via photo-Fenton oxidation. However, after 60-min UV irradiation, a peak at 1337 cm⁻¹, attributed to the disorder carbon structure [28], was significantly intensified in the Raman spectrum of Ag-CNT-M-FeOOH. It indicated the defective degrees of Ag-CNT-M-FeOOH increased after the photo-Fenton reaction. However, as exhibited in Fig. S6, the pore size distribution of the Ag-CNT-M-FeOOH membrane surface did not change much after 60-min UV treatment, implying the physical structural stability of the membrane during photo-Fenton oxidation.

From Fig. S7, we found a broad peak around 3340 cm⁻¹ due to the

hydroxyl groups in the ATR-FTIR spectra of Ag-CNT-M-FeOOH [54], and gradually enlarged as the UV treatment time increased. This is because that large quantities of reactive •OH species could be grafted onto Ag-CNT-M-FeOOH via electrophilic addition reaction [49], as schemed in Fig. 5d. The difference in T_2 of water before and after photo-catalytic treatment for the membrane surface was calculated as ΔT_2 in Fig. S8. The higher value of ΔT_2 , the better water affinity to the membrane surface [55]. The surface hydrophilicity of Ag-CNT-M-FeOOH with and without photo-Fenton oxidation treatment was also assessed by time-dependent water contact angle measurements. The pristine Ag-CNT-M-FeOOH slightly hydrophilic as its water contact angle declined from $72 \pm 1^\circ$ to $65 \pm 1^\circ$ in 60 s (Fig. 5d) due to the weak interaction with water. As the time of photo-Fenton oxidation treatment increased, the water contact angles declined to $38 \pm 1^\circ$ for the membrane after 60-min photo-catalytic treatment, indicating the enhanced surface hydrophilicity (Fig. 5d). The enhanced surface hydrophilicity of the membrane after photo-Fenton oxidation was caused by the surface-grafted hydroxyl

functional groups that promoted the strong hydrogen bonding between the membrane surface and water [55].

Fig. 5(e, f, and g) showed the results of recyclability studies on the dynamic adsorption of cationic dye (RhB) for the Ag-CNT-M-FeOOH membrane. Due to the improvement in hydrophilicity, the fluxes of the photo-treated Ag-CNT-M-FeOOH membrane increased significantly compared with its pristine fluxes within 180-min continuous filtration (Fig. 5e). The increased fluxes caused that more RhB molecules were adsorbed in the photo-treated Ag-CNT-M-FeOOH membrane, leading to an earlier achievement in membrane saturated adsorption. Therefore, RhB removal of the Ag-CNT-M-FeOOH membrane gradually decreased after five consecutive filtration cycles (Fig. 5f). However, the dynamic RhB removal of the Ag-CNT-M-FeOOH membrane was still at a high level after four times of regeneration. Fig. 5g showed the total RhB adsorption capacities of Ag-CNT-M-FeOOH after each cyclic separation. The total RhB adsorption capacity of Ag-CNT-M-FeOOH increased significantly after four times of regeneration. This result could be explained by that after photo-catalytic regeneration, more hydroxyl groups were grafted onto Ag-CNT-M-FeOOH, which enhanced the membrane electronegativity and thus its adsorption capacity to cationic RhB via the electrostatic attraction [36].

Table 1 showed the RhB adsorption kinetics of the Ag-CNT-M-FeOOH membrane after each regeneration. These results presented an ideal fit to the pseudo-first order kinetics for both pristine and all regenerated Ag-CNT-M-FeOOH membranes (with an extremely high $R^2 > 0.99$). The well fit to the pseudo-first order kinetics indicated that the adsorption mechanism mainly depended on the adsorbate and adsorbent [56]. The rate change in solute adsorption with time is directly proportional to the difference in saturation concentration and the amount of solid adsorption with time. There was little change in RhB concentration and physical structure of Ag-CNT-M-FeOOH during the five times of cyclic separation. Thus, it was expected that the increased hydrophilicity and electrostatic adsorption facilitated the adsorption of the membrane to the dye molecules. Correspondingly, the q_{e1} of Ag-CNT-M-FeOOH increased from 226 to 344 mg/g after five cycles (Table 1). This indicated that the Ag-CNT-M-FeOOH membrane exhibited excellent adsorption regeneration ability after the photo-Fenton oxidation treatment.

Table 1 also exhibited the MB, AO7, and EY adsorption kinetic results of the Ag-CNT-M-FeOOH membrane after twice regeneration, which were all fit well to the pseudo-first order kinetic with extremely high $R^2 > 0.99$. During the multi-regeneration process, the adsorption k_1 and q_{e1} of Ag-CNT-M-FeOOH for anionic dyes (AO7 and EY) were much lower than those of the membrane for cationic dyes (RhB and MB). It implied that the electric charge interaction between the CNT-based membrane and dyes played an important role in dye removal by dynamic adsorption.

During two cycles of regeneration, the Ag-CNT-M-FeOOH membrane was also employed to treat wastewater containing cation MB, anion AO7, and anion EY. Fig. 6a showed the fluxes of the pristine Ag-CNT-M-FeOOH membrane increased significantly from ~ 205 to ~ 267 L/m²·h, while the initial removal to dye molecules dropped from 100% for MB to

80% for EY after two cycles of regeneration. As discussed in Fig. S4, after each cycle of the photo-Fenton oxidation cleaning, the improved hydrophilicity in regenerated Ag-CNT-M-FeOOH (Reg-1 and Reg-2) could contribute to this flux rise. However, the cationic MB adsorption capacity of the pristine Ag-CNT-M-FeOOH membrane was very high (up to 247 mg/g) (Fig. 6b). It suggested that our Ag-CNT-M-FeOOH membrane had a stronger ability to purify cationic dye polluted wastewater via dynamic adsorption. Table 2 compared the maximum dye adsorption capacities of various CNT based adsorbents. Obviously, our Ag-CNT-FeOOH membrane had the highest adsorption capacities to both RhB and MB dyes among all the reported CNT based materials.

The regenerated Ag-CNT-FeOOH membrane (Reg-1 and Reg-2) displayed significantly reduced removal efficiencies for anionic AO7 and EY (Fig. 6a), suggesting their lower separation efficiencies for anionic dye polluted wastewater compared with those for cationic dye polluted water. The AO7 removal of Reg-1 sharply decreased from 91% to 17% during the 120-min continuous separation. At the end, the AO7 adsorption capacity of Reg-1 was much lower 153 mg/g (Fig. 6b) compared with the adsorption capacity for MB (247 mg/g). This result might be caused by the relatively low self-adsorption capacity of CNT for AO7 and the electrostatic repulsion between surface-grafted electro-negative compounds and AO7. Similarly, the EY removal of Reg-2 declined from 80% to 40% during the-120 min continuous separation. As calculated in Fig. 6b, the EY adsorption capacity of the membrane was 189 mg/g, which also lower than the dynamic adsorption capacity for cationic dye MB (247 mg/g). Moreover, dynamic adsorption experiments of the Ag-CNT-M-FeOOH membrane with two cyclic regenerations were also conducted for sequent removal of toxic aqueous AX, NP and BPA via the crossflow model and results were shown in Fig. S9.

Meanwhile, the Ag-CNT-M-FeOOH membrane exhibited high initial removals at $\sim 50\%$, $\sim 90\%$, and $\sim 100\%$ on the separation of AX, NP and BPA polluted water, respectively (Fig. S8a). The total adsorption capacities of the Ag-CNT-M-FeOOH membrane for AX, NP and BPA were 8, 7, and 13 mg/g on polluted water, respectively, as shown in Fig. S9b. These results indicated Ag-CNT-M-FeOOH membrane owned a certain efficiency on removing the small high-toxic pollutants from water, but the results needed to be improved.

Membrane fouling is an inevitable problem in all membrane separation processes for water purification. It can reduce water flux, deteriorate product water quality, increase energy consumption and shorten membrane lifespans due to cleaning [18]. For this reason, we employed an advanced photo-catalytic cleaning technology to reduce membrane fouling. As shown in Fig. 7, the pure water flux of Ag-CNT-M-FeOOH was around ~ 230 L/m²·h during the first 60-min continuous filtration. The flux of Ag-CNT-M-FeOOH sharply decreased to ~ 38 L/m²·h when pure water was changed into the BSA solution (1 g/L). Such serious BSA fouling of the Ag-CNT-M-FeOOH membrane was mainly caused by surface adsorption, pore blocking and cake layer deposition of the BSA protein via the protein-membrane and protein-protein interactions, since the membrane had a relatively large pore size (Fig. 3). Water transport pathways of the membrane were blocked by the BSA

Table 1
Fitting data of adsorption kinetics for Ag-CNT-M-FeOOH.

Adsorbent	Recycle Index	Pollutant	q_e (exp)	Pseudo-first-order			
				k_1 (min ⁻¹)	q_{e1} (mg·g ⁻¹)	R^2	
Ag-CNT-M-FeOOH	0	RhB	181.7920	0.0094	226.3008	0.9999	
	1		209.8737	0.0109	249.0047	0.9988	
	2		219.1948	0.0135	244.0414	0.9990	
	3		290.7423	0.0138	321.1793	0.9979	
	4		317.4696	0.0126	344.1573	0.9991	
	0	MB	254.9935	0.0201	394.0558	0.9996	
	1		159.3765	0.0086	169.0838	0.9955	
	2		189.3942	0.0040	193.0625	0.9987	
			AO7				
			EY				

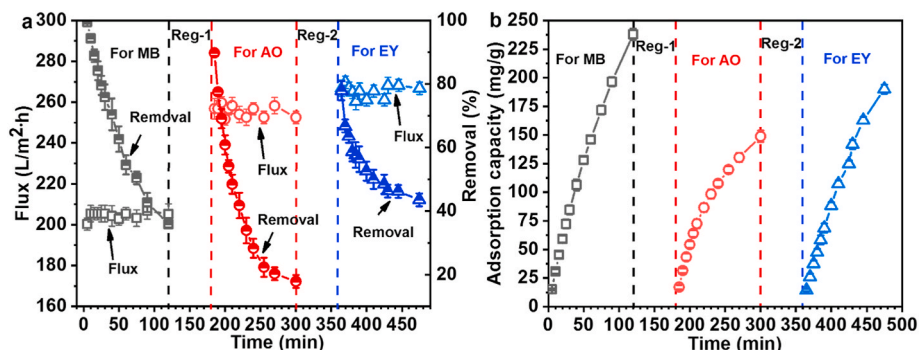


Fig. 6. (a) The flux and removal, and (b) adsorption capacity of Ag-CNT-M-FeOOH for consecutive MB (20 ppm), AO7 (20 ppm) and EY (20 ppm) separation with two regeneration cycles.

Table 2

Comparison in dye adsorption capacities of different CNT based adsorbents/adsorptive membranes from literature.

Adsorbents/adsorptive membranes	Dyes	q _e (mg/g)	References
Bentonite-carbon nanotube nanocomposite	RhB (200 ppm)	142.8	[21]
MWCNT-COOH	RhB (1000 ppm)	42.68	[19]
Ferrocene-modified MWCNTs	RhB (20 ppm)	98	[57]
CNT membrane	RhB (10 ppm)	32.5	[58]
Ag-CNT-FeOOH membrane	RhB (20 ppm)	181	This work
MWCNT buckypaper/polyvinyl alcohol membrane	MB (20 ppm)	30	[59]
Magnetic graphene-MWCNT composite	MB (10 ppm)	65.79	[22]
Poly(ionic liquid) membrane	MB (10 ppm)	N/A (94.5% removal)	[60]
PVDF-TiO ₂ membrane	MB (50 ppm)	N/A (93.1%)	[61]
GO/polysulphone membrane	MB (20 ppm)	1.8	[62]
Ag-CNT-FeOOH membrane	MB (20 ppm)	247	This work

protein, leading to significant water flux reduction. To recover water flux, we first used the conventional pure water cleaning for the fouled Ag-CNT-M-FeOOH membrane by backwashing. After pure water cleaning, the pure water flux of Ag-CNT-M-FeOOH was recovered to 207 L/m²·h, about 90% of the original pure water flux. The physical water cleaning could not remove all BSA foulants within the Ag-CNT-M-FeOOH membrane.

After the second cycle of BSA fouling, the permeation flux reduced to the similar level as that in the first cycle (37 L/m²·h). We employed a photo-catalytic cleaning for the BSA fouled Ag-CNT-M-FeOOH membrane. The flux recovery of the Ag-CNT-M-FeOOH membrane was slightly over 100%. The possible reasons have been discussed above, including the increased hydrophilicity and affinity to water molecules caused by the surface-grafted hydroxyl functional groups that promoted the strong hydrogen bonding (hydration layer). In addition, the active •OH radicals could precisely generate on foulant-membrane interfaces via AOPs of catalytic membrane, which largely reduce the interaction between the foulant and the membrane [49]. Subsequently, the foulant can be easily removed from the membrane and lead to high flux recovery. The BSA flux of Ag-CNT-M-FeOOH also increased to 50 L/m²·h. The second photo-catalytic cleaning further improved the pure water flux of Ag-CNT-M-FeOOH to 320 L/m²·h. It indicated that the photo-catalytic cleaning further imparted more active •OH radicals grafting onto the Ag-CNT-M-FeOOH membrane for the improvement of the membrane permeation and BSA fouling resistance.

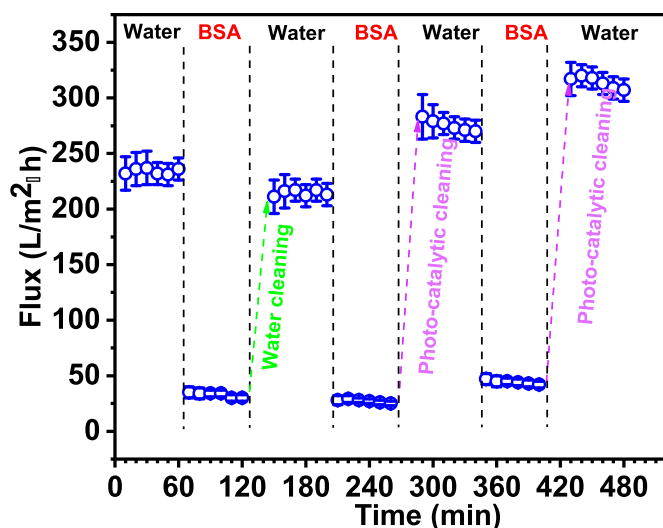


Fig. 7. Permeation fluxes with pure water and BSA solution (1 g/L) of Ag-CNT-M-FeOOH and the membrane photo-regenerative property during the fouling-cleaning cycles.

4. Conclusions

In this work, we developed a highly adsorptive self-cleaning carbon nanotube based membrane (Ag-CNT-FeOOH membrane) via the facile vacuum filtration method followed by silver-amino reaction. The Ag-CNT-FeOOH membrane showed improved robustness due to the welding of nanoparticles on the membrane surface by silver-amino reaction. In dynamic filtration, our membrane exhibited superior adsorption performance among CNT based adsorbents reported in literature. For example, the adsorption capacities of the membrane for RhB and MB dyes were up to 181 and 247 mg/g, respectively. In particular, the Ag-CNT-FeOOH composite membrane displayed even better adsorption performance to cationic dyes (e.g. MB). Our membrane also had excellent self-cleaning and photo-regenerable properties after severe organic fouling. The high separation performance and self-cleaning properties of the membrane can be explained by the enhanced surface hydrophilicity and the reactive •OH species grafted onto the membrane. This study offers a new strategy to engineer robust adsorptive, self-cleaning and regenerable membrane for dye polluted wastewater purification.

CRediT authorship contribution statement

Yang Yang: Data curation, Investigation, Methodology, Writing -

original draft. **Zhu Xiong**: Data curation, Investigation, Funding acquisition, Writing - review & editing. **Zhu Wang**: Investigation, Methodology, Writing - review & editing. **Yi Liu**: Methodology, Conceptualization, Writing - review & editing. **Zijun He**: Investigation, Methodology. **Akun Cao**: Data curation, Methodology. **Li Zhou**: Methodology. **Lijing Zhu**: Data curation, Methodology. **Shuaifei Zhao**: Methodology, Conceptualization, Supervision, Writing - review & editing.

Declaration of competing interest

The authors declare that they have no known competing financial interests or personal relationships that could have appeared to influence the work reported in this paper.

Acknowledgements

This work was supported by the National Natural Science Foundation of China (51808142, 51538013), the National Key Research and Development Plan (2016YFA0203200), the introduced innovative R & D team project under the “The Pearl River Talent Recruitment Program” of Guangdong Province, Science and Technology Research Project of Guangzhou (201904010217), State Key Laboratory of Pollution Control and Resource Reuse Foundation (PCRRF19010), Scientific Project of Guangzhou University (YG2020020) and Science Starting Foundation of Guangzhou University (BX20006272).

Appendix A. Supplementary data

Supplementary data to this article can be found online at <https://doi.org/10.1016/j.memsci.2020.119000>.

References

- [1] M. Jiang, K. Ye, J. Deng, J. Lin, W. Ye, S. Zhao, B. Van der Bruggen, Conventional ultrafiltration as effective strategy for dye/salt fractionation in textile wastewater treatment, *Environ. Sci. Technol.* 52 (2018) 10698–10708.
- [2] M. Jiang, K. Ye, J. Lin, X. Zhang, W. Ye, S. Zhao, B. Van der Bruggen, Effective dye purification using tight ceramic ultrafiltration membrane, *J. Membr. Sci.* 566 (2018) 151–160.
- [3] Y. Wei, H. Qi, X. Gong, S. Zhao, Specially wettable membranes for oil–water separation, *Adv. Mater. Interfaces* 5 (2018), 1800576.
- [4] P.A. Carneiro, G.A. Umbuzeiro, D.P. Oliveira, M.V.B. Zanoni, Assessment of water contamination caused by a mutagenic textile effluent/dyehouse effluent bearing disperse dyes, *J. Hazard Mater.* 174 (2010) 694–699.
- [5] J. Choina, H. Kosslick, C. Fischer, G.U. Flechsig, L. Frunza, A. Schulz, Photocatalytic decomposition of pharmaceutical ibuprofen pollution in water over titania catalyst, *Appl. Catal. B Environ.* 129 (2013) 589–598.
- [6] J. Fenoll, P. Flores, P. Hellín, C.M. Martínez, S. Navarro, Photodegradation of eight miscellaneous pesticides in drinking water after treatment with semiconductor materials under sunlight at pilot plant scale, *Chem. Eng. J.* 204–206 (2012) 54–64.
- [7] Y.-T. Zuo, Y. Hu, W.-W. Lu, J.-J. Cao, F. Wang, X. Han, W.-Q. Lu, A.-L. Liu, Toxicity of 2,6-dichloro-1,4-benzoquinone and five regulated drinking water disinfection by-products for the *Caenorhabditis elegans* nematode, *J. Hazard Mater.* 321 (2017) 456–463.
- [8] A. Szczuka, K.M. Parker, C. Harvey, E. Hayes, A. Vengosh, W.A. Mitch, Regulated and unregulated halogenated disinfection byproduct formation from chlorination of saline groundwater, *Water Res.* 122 (2017) 633–644.
- [9] M.M. Pendergast, E.M.V. Hoek, A review of water treatment membrane nanotechnologies, *Energy Environ. Sci.* 4 (2011) 1946–1971.
- [10] R. Lamsal, M.E. Walsh, G.A. Gagnon, Comparison of advanced oxidation processes for the removal of natural organic matter, *Water Res.* 45 (2011) 3263–3269.
- [11] X. Zhang, X. Fang, J. Li, S. Pan, X. Sun, J. Shen, W. Han, L. Wang, S. Zhao, Developing new adsorptive membrane by modification of support layer with iron oxide microspheres for arsenic removal, *J. Colloid Interface Sci.* 514 (2018) 760–768.
- [12] W. Ye, H. Liu, M. Jiang, J. Lin, K. Ye, S. Fang, Y. Xu, S. Zhao, B. Van der Bruggen, Z. He, Sustainable management of landfill leachate concentrate through recovering humic substance as liquid fertilizer by loose nanofiltration, *Water Res.* 157 (2019) 555–563.
- [13] C. Li, G. Feng, Z. Pan, C. Song, X. Fan, P. Tao, T. Wang, M. Shao, S. Zhao, High-performance electrocatalytic microfiltration CuO/Carbon membrane by facile dynamic electrodeposition for small-sized organic pollutants removal, *J. Membr. Sci.* 601 (2020), 117913.
- [14] Y.-l. Liu, X.-m. Wang, H.-w. Yang, Y.F. Xie, X. Huang, Preparation of nanofiltration membranes for high rejection of organic micropollutants and low rejection of divalent cations, *J. Membr. Sci.* 572 (2019) 152–160.
- [15] A. Ben-David, R. Bernstein, Y. Oren, S. Belfer, C. Dosoretz, V. Freger, Facile surface modification of nanofiltration membranes to target the removal of endocrine-disrupting compounds, *J. Membr. Sci.* 357 (2010) 152–159.
- [16] N.K. Khanzada, M.U. Farid, J.A. Kharraz, J. Choi, C.Y. Tang, L.D. Nghiem, A. Jang, A.K. An, Removal of organic micropollutants using advanced membrane-based water and wastewater treatment: a review, *J. Membr. Sci.* 598 (2020), 117672.
- [17] S. Zhao, L. Zou, C.Y. Tang, D. Mulcahy, Recent developments in forward osmosis: opportunities and challenges, *J. Membr. Sci.* 396 (2012) 1–21.
- [18] R. Zhang, Y. Liu, M. He, Y. Su, X. Zhao, M. Elimelech, Z. Jiang, Antifouling membranes for sustainable water purification: strategies and mechanisms, *Chem. Soc. Rev.* 45 (2016) 5888–5924.
- [19] O.A. Oyedate, V.O. Nyamori, B.S. Martincigh, S.B. Jonnalagadda, Effectiveness of carbon nanotube–cobalt ferrite nanocomposites for the adsorption of rhodamine B from aqueous solutions, *RSC Adv.* 5 (2015) 22724–22739.
- [20] M. Sui, S. Xing, L. Sheng, S. Huang, H. Guo, Heterogeneous catalytic ozonation of ciprofloxacin in water with carbon nanotube supported manganese oxides as catalyst, *J. Hazard Mater.* 227–228 (2012) 227–236.
- [21] M.I. Mohammed, S. Baytak, Synthesis of bentonite–carbon nanotube nanocomposite and its adsorption of rhodamine dye from water, *Arabian J. Sci. Eng.* 41 (2016) 4775–4785.
- [22] P. Wang, M. Cao, C. Wang, Y. Ao, J. Hou, J. Qian, Kinetics and thermodynamics of adsorption of methylene blue by a magnetic graphene-carbon nanotube composite, *Appl. Surf. Sci.* 290 (2014) 116–124.
- [23] M. Gong, Y. Li, H. Wang, Y. Liang, J.Z. Wu, J. Zhou, J. Wang, T. Regier, F. Wei, H. Dai, An advanced Ni–Fe layered double hydroxide electrocatalyst for water oxidation, *J. Am. Chem. Soc.* 135 (2013) 8452–8455.
- [24] Z. Shi, W. Zhang, F. Zhang, X. Liu, D. Wang, J. Jin, L. Jiang, Ultrafast separation of emulsified oil/water mixtures by ultrathin free-standing single-walled carbon nanotube network films, *Adv. Mater.* 25 (2013) 2422–2427.
- [25] H. Huang, Y. Ying, X. Peng, Graphene oxide nanosheet: an emerging star material for novel separation membranes, *J. Mater. Chem.* 2 (2014) 13772–13782.
- [26] R. Das, M.E. Ali, S.B.A. Hamid, S. Ramakrishna, Z.Z. Chowdhury, Carbon nanotube membranes for water purification: a bright future in water desalination, *Desalination* 336 (2014) 97–109.
- [27] H.Y. Yang, Z.J. Han, S.F. Yu, K.L. Pey, K. Ostrikov, R. Karnik, Carbon nanotube membranes with ultrahigh specific adsorption capacity for water desalination and purification, *Nat. Commun.* 4 (2013) 2220.
- [28] Z. Chen, S. Mahmud, L. Cai, Z. He, Y. Yang, L. Zhang, S. Zhao, Z. Xiong, Hierarchical poly(vinylidene fluoride)/active carbon composite membrane with self-confining functional carbon nanotube layer for intractable wastewater remediation, *J. Membr. Sci.* 603 (2020), 118041.
- [29] J. Luan, P.-X. Hou, C. Liu, C. Shi, G.-X. Li, H.-M. Cheng, Efficient adsorption of organic dyes on a flexible single-wall carbon nanotube film, *J. Mater. Chem.* 4 (2016) 1191–1194.
- [30] Q. Liu, S. Huang, Y. Zhang, S. Zhao, Comparing the antifouling effects of activated carbon and TiO₂ in ultrafiltration membrane development, *J. Colloid Interface Sci.* 515 (2018) 109–118.
- [31] Y. Li, S. He, Z. Zhou, S. Zhou, S. Huang, A.G. Fane, C. Zheng, Y. Zhang, S. Zhao, Carboxylated nanodiamond-enhanced photocatalytic membranes with improved antifouling and self-cleaning properties, *Ind. Eng. Chem. Res.* 59 (2020) 3538–3549.
- [32] H. Yu, J. Huang, L. Jiang, Y. Shi, K. Yi, W. Zhang, J. Zhang, H. Chen, X. Yuan, Enhanced photocatalytic tetracycline degradation using N-CQDs/OV-BiOBr composites: unraveling the complementary effects between N-CQDs and oxygen vacancy, *Chem. Eng. J.* 402 (2020), 126187.
- [33] Y. Shi, J. Huang, G. Zeng, W. Cheng, J. Hu, Photocatalytic membrane in water purification: is it stepping closer to be driven by visible light? *J. Membr. Sci.* 584 (2019) 364–392.
- [34] Z. Xiong, T. Li, F. Liu, H. Lin, Y. Zhong, Q.a. Meng, Q. Fang, H. Sakil, W. Song, Chinese knot inspired Ag nanowire membrane for robust separation in water remediation, *Adv. Mater. Interfaces* 5 (2018), 1800183.
- [35] Z. Xiong, H. Lin, F. Liu, X. Yu, Y. Wang, Y. Wang, A new strategy to simultaneously improve the permeability, heat-deformation resistance and antifouling properties of polylactide membrane via bio-based β -cyclodextrin and surface crosslinking, *J. Membr. Sci.* 513 (2016) 166–176.
- [36] V. Vimonses, S. Lei, B. Jin, C.W.K. Chow, C. Saint, Kinetic study and equilibrium isotherm analysis of Congo Red adsorption by clay materials, *Chem. Eng. J.* 148 (2009) 354–364.
- [37] Z. He, S. Mahmud, Y. Yang, L. Zhu, Y. Zhao, Q. Zeng, Z. Xiong, S. Zhao, Polyvinylidene fluoride membrane functionalized with zero valent iron for highly efficient degradation of organic contaminants, *Separ. Purif. Technol.* 250 (2020), 117266.
- [38] Q. Ding, W.U. Khan, F.L.Y. Lam, Y. Zhang, S. Zhao, A.C.K. Yip, X. Hu, Graphitic carbon nitride/copper-iron oxide composite for effective Fenton degradation of ciprofloxacin at near-neutral pH, *ChemistrySelect* 5 (2020) 8198–8206.
- [39] W. Ye, H. Liu, F. Lin, J. Lin, S. Zhao, S. Yang, J. Hou, S. Zhou, B. Van der Bruggen, High-flux nanofiltration membranes tailored by bio-inspired co-deposition of hydrophilic g-C₃N₄ nanosheets for enhanced selectivity towards organics and salts, *Environ. Sci.: Nano* 6 (2019) 2958–2967.
- [40] H. Sun, C. Kwan, A. Suvorova, H.M. Ang, M.O. Tadé, S. Wang, Catalytic oxidation of organic pollutants on pristine and surface nitrogen-modified carbon nanotubes with sulfate radicals, *Appl. Catal. B Environ.* 154–155 (2014) 134–141.

- [41] X. Qian, Y. Wu, M. Kan, M. Fang, D. Yue, J. Zeng, Y. Zhao, FeOOH quantum dots coupled g-C₃N₄ for visible light driving photo-Fenton degradation of organic pollutants, *Appl. Catal. B Environ.* 237 (2018) 513–520.
- [42] H. Li, Q. Zhou, F. Liu, W. Zhang, Z. Tan, H. Zhou, Z. Huang, S. Jiao, Y. Kuang, Biomimetic design of ultrathin edge-riched FeOOH@Carbon nanotubes as high-efficiency electrocatalysts for water splitting, *Appl. Catal. B Environ.* 255 (2019), 117755.
- [43] Y. Liu, X. Liu, Y. Zhao, D.D. Dionysiou, Aligned α -FeOOH nanorods anchored on a graphene oxide-carbon nanotubes aerogel can serve as an effective Fenton-like oxidation catalyst, *Appl. Catal. B Environ.* 213 (2017) 74–86.
- [44] A. Gautam, P. Tripathy, S. Ram, Microstructure, topology and X-ray diffraction in Ag-metal reinforced polymer of polyvinyl alcohol of thin laminates, *J. Mater. Sci.* 41 (2006) 3007–3016.
- [45] B. Jachimska, M. Wasilewska, Z. Adamczyk, Characterization of globular protein solutions by dynamic light scattering, electrophoretic mobility, and viscosity measurements, *Langmuir* 24 (2008) 6866–6872.
- [46] J.-f. Liu, Z.-s. Zhao, G.-b. Jiang, Coating Fe₃O₄ magnetic nanoparticles with humic acid for high efficient removal of heavy metals in water, *Environ. Sci. Technol.* 42 (2008) 6949–6954.
- [47] Y. Zhong, T. Li, H. Lin, L. Zhang, Z. Xiong, Q. Fang, G. Zhang, F. Liu, Meso-/macro-porous microspheres confining Au nanoparticles based on PDLA/PLLA stereo-complex membrane for continuous flowing catalysis and separation, *Chem. Eng. J.* 344 (2018) 299–310.
- [48] J.-H. Huang, K.-L. Huang, S.-Q. Liu, A.T. Wang, C. Yan, Adsorption of Rhodamine B and methyl orange on a hypercrosslinked polymeric adsorbent in aqueous solution, *Colloid. Surface. Physicochem. Eng. Aspect.* 330 (2008) 55–61.
- [49] Z. He, S. Mahmud, S. Zhao, Y. Yang, L. Zhu, Y. Zhao, Q. Zeng, Z. Xiong, C. Hu, Hierarchically active poly(vinylidene fluoride) membrane fabricated by in situ generated zero-valent iron for fouling reduction, *ACS Appl. Mater. Interfaces* 12 (2020) 10993–11004.
- [50] H. Lin, Q. Fang, W. Wang, G. Li, J. Guan, Y. Shen, J. Ye, F. Liu, Prussian blue/PVDF catalytic membrane with exceptional and stable Fenton oxidation performance for organic pollutants removal, *Appl. Catal. B Environ.* 273 (2020), 119047.
- [51] X. Zuo, M. Chen, D. Fu, H. Li, The formation of alpha-FeOOH onto hydrothermal biochar through H₂O₂ and its photocatalytic disinfection, *Chem. Eng. J.* 294 (2016) 202–209.
- [52] X. Qian, M. Ren, Y. Zhu, D. Yue, Y. Han, J. Jia, Y. Zhao, Visible light assisted heterogeneous fenton-like degradation of organic pollutant via α -FeOOH/mesoporous carbon composites, *Environ. Sci. Technol.* 51 (2017) 3993–4000.
- [53] Z.-L. Wang, Z.-H. Kang, E.-B. Wang, Z.-M. Su, L. Xu, Intercalation and photophysical properties of the tetra-(8-hydroxyquinolino) boron complex and 3,3',4,4'-benzophenone tetracarboxylic anion into Mg–Al layered double hydroxides, *Inorg. Chem.* 45 (2006) 4364–4371.
- [54] A. Burneau, O. Barres, J.P. Gallas, J.C. Lavalley, Comparative study of the surface hydroxyl groups of fumed and precipitated silicas. 2. Characterization by infrared spectroscopy of the interactions with water, *Langmuir* 6 (1990) 1364–1372.
- [55] J. Wu, W. Lin, Z. Wang, S. Chen, Y. Chang, Investigation of the hydration of nonfouling material poly(sulfobetaine methacrylate) by low-field nuclear magnetic resonance, *Langmuir* 28 (2012) 7436–7441.
- [56] F.A. Pavan, S.L.P. Dias, E.C. Lima, E.V. Benvenutti, Removal of Congo red from aqueous solution by anilinepropylsilica xerogel, *Dyes Pigments* 76 (2008) 64–69.
- [57] A. Rabti, A. Hannachi, H. Maghraoui-Meherzi, N. Raouafi, Ferrocene-Functionalized carbon nanotubes: an adsorbent for rhodamine B, *Chem. Afr.* 2 (2019) 113–122.
- [58] G. Wei, H. Yu, X. Quan, S. Chen, H. Zhao, X. Fan, Constructing all carbon nanotube hollow fiber membranes with improved performance in separation and antifouling for water treatment, *Environ. Sci. Technol.* 48 (2014) 8062–8068.
- [59] L.Y. Jun, R.R. Karri, N.M. Mubarak, L.S. Yon, C.H. Bing, M. Khalid, P. Jagadish, E. C. Abdullah, Modelling of methylene blue adsorption using peroxidase immobilized functionalized Buckypaper/polyvinyl alcohol membrane via ant colony optimization, *Environ. Pollut.* 259 (2020), 113940.
- [60] A. Wu, F. Lu, M. Zhao, N. Sun, L. Shi, L. Zheng, Photo and humidity responsive mesoporous poly(ionic liquid) membrane for selective dye adsorption, *ChemistrySelect* 2 (2017) 1878–1884.
- [61] H.P. Ngang, B.S. Ooi, A.L. Ahmad, S.O. Lai, Preparation of PVDF-TiO₂ mixed-matrix membrane and its evaluation on dye adsorption and UV-cleaning properties, *Chem. Eng. J.* 197 (2012) 359–367.
- [62] W. Shi, X. Zeng, H. Li, R. Zhou, H. Zhang, X. Qin, Preparation of carboxylated graphene oxide nanosheets/polysulphone hollow fibre separation membranes with improved separation and dye adsorption properties, *Color. Technol.* 135 (2019) 370–382.